

Broadband biphoton generation and polarization splitting in a monolithic AlGaAs chip

Félicien Appas,^{†,‡,||} Othmane Meskine,^{†,||} Aristide Lemaître,[¶] José Palomo,[§]
Florent Baboux,[†] Maria I. Amanti,^{*,†} and Sara Ducci^{*,†}

[†]*Université Paris Cité, CNRS, Laboratoire Matériaux et Phénomènes Quantiques, 75013 Paris, France*

[‡]*Current address: ICFO - Institut de Ciències Fotoniques, The Barcelona Institute of Science and Technology, Castelldefels (Barcelona) 08860, Spain*

[¶]*Université Paris-Saclay, CNRS, Centre de Nanosciences et de Nanotechnologies, 91120, Palaiseau, France*

[§]*Laboratoire de Physique de l'École normale supérieure, ENS, Université PSL, CNRS, Sorbonne Université, Université Paris Cité, F-75005 Paris, France*

^{||}*These authors contributed equally to this work*

E-mail: maria.amanti@u-paris.fr; sara.ducci@u-paris.fr

Abstract

The ability to combine various advanced functionalities on a single chip is a key issue for both classical and quantum photonic-based technologies. On-chip generation and handling of orthogonally polarized photon pairs, one of the most used resources in quantum information protocols, is a central challenge for the development of scalable quantum photonics circuits; in particular, the management of spectrally broadband biphoton states, an asset attracting a growing attention for its capability to convey large-scale quantum information in a single spatial mode, is missing. Here, we demonstrate a monolithic AlGaAs chip including the generation of broadband orthogonally polarized photon pairs and their polarization splitting; 85% of the pairs are deterministically separated by the chip over a 60 nm bandwidth. The quality of the two-photon interference at the chip output is assessed via a Hong-Ou-Mandel experiment displaying a raw visibility of 75.5% over the same bandwidth. These results, obtained

for the first time at room temperature and telecom wavelength, in a platform combining strong confinement, high second-order nonlinearity, electro-optic effect and direct bandgap, confirm the validity of our approach and represent a significant step towards miniaturized and easy-to-handle photonic devices working in the broadband regime for quantum information processing.

Introduction

Photonic quantum technologies are a valuable approach for quantum information processing including secure communications, quantum computation, simulation and metrology.^{1,2} While quantum photonic experiments in bulk optics continue to produce important results demonstrating the advantage of quantum technologies over classical ones in several domains,³⁻⁶ integration at the chip scale has become essential to scale up these concepts and transform laboratory demonstrators into real-world technologies.^{7,8} In the last two decades,

significant advances on integrated quantum photonic circuits have enabled the generation and manipulation of quantum states of light at an increasing scale and level of complexity exploiting a variety of optical material platforms. Most of these achievements have been done using glass or indirect-bandgap $\chi^{(3)}$ materials such as silicon nitride, silicon-on-insulator or silica on silicon,⁹ despite the fact that the use of $\chi^{(2)}$ materials leads to more efficient frequency conversion processes and allow for easy pump filtering. Important results using this second class of materials have been obtained with lithium niobate-based photonics circuits, having led to the demonstration of an on-chip squeezing experiment,^{10,11} a two-channel spectrally degenerate polarization entangled source¹² and a nonlinear integrated quantum electro-optic device.¹³ However, in the first two works the chip doesn't manage polarization, while in the third and fourth ones the devices work in a narrow spectral bandwidth regime and have typical sizes of several centimeters. Polarization handling of broadband biphoton states on miniature chips would constitute a crucial resource in the toolbox of integrated quantum photonic circuits. Indeed, on the one hand polarization is one of the most used degrees of freedom in quantum information protocols, widely employed both for deterministic separation of photons or to encode entanglement; on the other hand, broadband frequency states for high-dimensional encoding are attracting a growing interest thanks to their capability to convey large-scale quantum information into a single spatial mode,¹⁴ an important asset for scalability. Although broadband integrated polarization mode splitters working in the classical regime have been demonstrated in Si-based platforms,^{15–17} polymers¹⁸ and lithium niobate waveguide circuits,¹⁹ to date, there exists no device able to combine the generation of broadband biphoton states and their deterministic splitting through polarization. Moreover, to combine these two very distinct functionalities in a simple monolithic design that requires only very few fabrication steps is a significant technological challenge.

Here, we demonstrate a monolithic AlGaAs

waveguide circuit including the generation of broadband orthogonally polarized photon pairs via type II spontaneous parametric down conversion and their polarization splitting through a birefringent directional coupler. AlGaAs waveguides are a promising all-rounder physical platform for quantum photonics that stands out among other systems by combining at the same time strong light confinement, high $\chi^{(2)}$ (150 pm V⁻¹ at 1550 nm) and electro-optic coefficient,²⁰ moderate propagation losses and compliance with electrical injection.²¹ A comparison between the properties of AlGaAs and other materials for quantum photonics can be found in Ref.²² We demonstrate that 85% of the pairs are deterministically spatially separated via their polarization over a bandwidth of 60 nm. The performances of the device as a quantum photonic circuit are assessed by implementing a Hong-Ou-Mandel interferometer at the chip output, one of the fundamental experiments in quantum optics lying at the heart of many nonclassical logic operations; the obtained visibility is 75.5% for a 60 nm-broad biphoton state. These results, obtained at room temperature and telecom wavelength in a material platform exhibiting valuable miniaturization and optoelectronic capabilities, represent a significant step towards real-world quantum photonic integrated circuits working in the broadband regime.

Sample layout and classical characterization

The device, sketched in Fig. 1 (a), combines a parametric source of orthogonally-polarized photon-pairs followed by a broadband polarizing mode splitter fabricated out of an epitaxially-grown multilayer AlGaAs wafer by a one-step inductively coupled plasma etching process (see Supplementary Material for details). In this design the generation region and the polarization splitter consist of two monolithic waveguides of variable width converging at a central evanescent coupling region through S-Bend waveguides. The integration of the two functionalities on the same monolithic chip re-

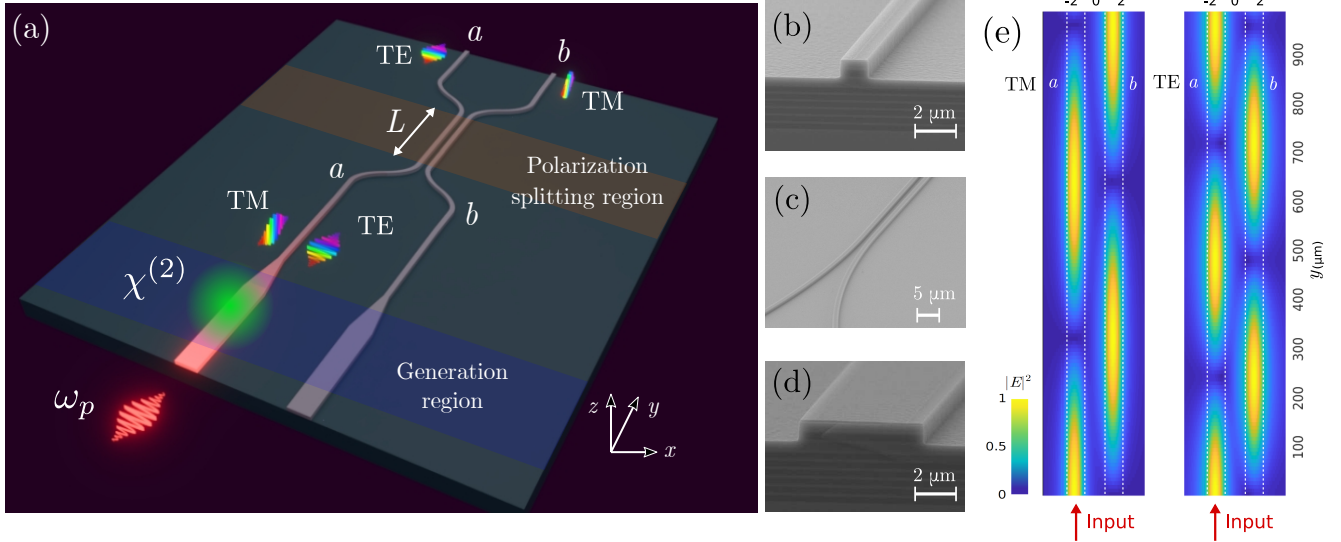


Figure 1: (a) Chip layout showing the photon-pair generation region and the polarization splitting region. (b-d) SEM images of the fabricated sample. (b) Output waveguide section, (c) S-Bends and polarization splitting region, (d) generation region waveguide section. (e) Electromagnetic simulation of the square modulus of the electric field in the polarization splitting region for light propagating in the fundamental TE and TM modes in a nominal structure.

quired a specific development for both the epitaxial structure and the design of the photonic circuit in order to meet the constraints related to the fabrication process and to the control on the generated quantum state as will be explained in the following.

Photon pairs in the telecom S+C band are generated into a 5 μm -wide ridge waveguide section which is then tapered down to a narrower width w when approaching the polarization splitting region. In this part of the chip, the waveguides are separated by a gap g and evanescent coupling occurs between the guided modes of the two structures. We design the device by defining w , g as well as the coupling length L such that photons generated in the TM mode, with an electric field along the z -axis, are coupled into the opposite waveguide, while photons generated in the TE mode, with an electric field along the x -axis, exit through the injection waveguide itself. The device was patterned by electron-beam lithography and dry etched by inductively coupled plasma (ICP) leading to a ridge height of 800 nm (see Supplementary Material for details). Scanning electron micrographs of the chip input, output and S-Bends regions, showing high fabrication quality

with upright and smooth waveguide sidewalls, are featured in Fig. 1 (b-d).

The generation region is based on a Bragg reflection waveguide emitting photon-pairs through Type II spontaneous parametric down-conversion (SPDC).^{23,24} We note that a specific design of the epitaxial structure of the chip has been necessary in order to cope with the fabrication issues of the splitting region. Indeed, the main drawback of the dry etching technique used to process the chip is that the etching rate is lower in the narrow gap between waveguides within the splitting region than in the rest of the chip. Numerical simulations showed that using the conventional 6-layer Bragg reflector AlGaAs waveguides described in Refs.^{24,25} the height unbalance between the inter-waveguide gap and the outer sidewalls accumulated during the etching time would prevent reaching a high splitting ratio. We solved this issue by designing an epitaxial structure featuring the same nonlinear conversion efficiency but having only two upper Bragg reflectors²² (as can be seen in Fig. 1 (b,d)) thus requiring a much shorter etch time. This results in a more uniform etching profile across the structure allowing for optimal splitting ratios. The chip is pumped by an ex-

ternal CW near-infrared laser. Typical internal pair generation rate and brightness of a 2 mm-long straight waveguide having the same epitaxial structure are 7×10^6 pairs/s and 2×10^5 pairs/s/mW/nm (in terms of internal pump power) respectively, placing the AlGaAs platform at the state-of-the-art level for integrated sources of polarization-entangled photons.²² The very short length of the waveguides that stems from the high $\chi^{(2)}$ of GaAs combined with the intrinsically low group velocity mismatch between orthogonally polarized modes of the waveguides allows for the generation of photon pairs entangled in the frequency and polarization degrees of freedom without the need for off-chip temporal walk-off compensation.^{22,24,25} Another key property of the source is its wide spectral bandwidth (60 nm)²⁶ and strongly anticorrelated joint spectral amplitude²² making it ideal for multi-user entanglement based QKD networks or high-dimensional frequency-based quantum information.^{25,26} In this kind of structure, the SPDC phase-matching wavelength depends on the effective refractive index of the involved modes and consequently on the waveguide width. This property has been judiciously exploited in the design of the chip to prevent the spurious generation of photon pairs in the polarization splitting region and the output arms. By varying the waveguides width along the propagation direction throughout the device, we ensure that the pump is tuned to the phase-matching wavelength in the generation region (762.5 nm for the 5 μm -wide waveguide), while it is detuned in the polarization splitting region and output arms of the device (770.5 nm for the 1.5 μm -wide waveguide) and will therefore not trigger the SPDC process.

The polarization splitting region relies on a birefringent directional coupler architecture. We denote by $\mathbf{E}_a, \mathbf{E}_b$ the electromagnetic field of the fundamental modes of waveguides a and b , as indicated in Fig. 1 (a). Following the coupled modes theory,²⁷ in the evanescent coupling region the eigenmodes of the structure take the form of symmetric S and anti-symmetric AS supermodes : $\mathbf{E}_S = (\mathbf{E}_a + \mathbf{E}_b)/\sqrt{2}$ and $\mathbf{E}_{AS} = (\mathbf{E}_a - \mathbf{E}_b)/\sqrt{2}$ with associated propagation constants β_S and β_{AS} . As a result, light

propagating along the y axis in the TE (resp. TM) fundamental mode of waveguide a will hop back and forth between the two evanescently coupled waveguides with a beating length $L_b^{(\text{TE})} = \pi/(\beta_S^{\text{TE}} - \beta_{AS}^{\text{TE}})$ (resp. $L_b^{(\text{TM})} = \pi/(\beta_S^{\text{TM}} - \beta_{AS}^{\text{TM}})$). Thanks to the intrinsic modal birefringence of the waveguides, we can find a region in the parameter space (w, g) for which:

$$\frac{L_b^{(\text{TE})}}{L_b^{(\text{TM})}} = \frac{p}{p+1}. \quad (1)$$

where p is an integer. In our case, we have chosen $p = 3$. When this condition is met, we choose a coupling length $L = 4L_b^{(\text{TE})}$ such that incoming TE-polarized light in waveguide a is totally transferred to output port a after hopping four times between the waveguides, while TM-polarized light undergoes three hops before exiting through the opposite output port b .

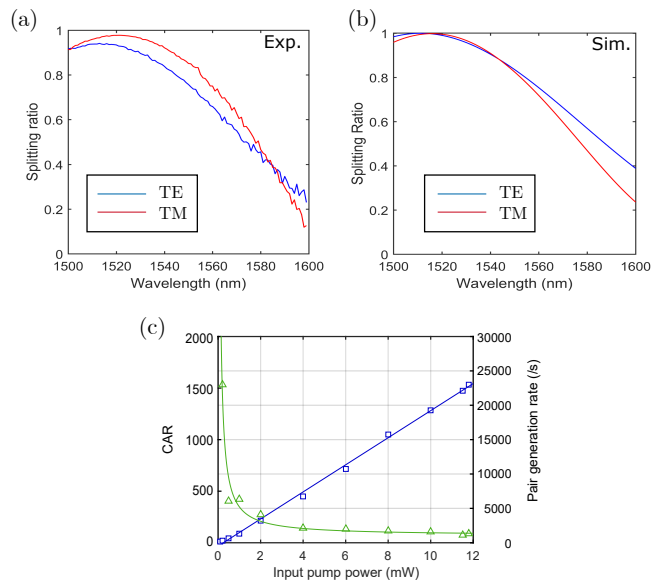


Figure 2: (a) Measured $s_{\text{TE}}, s_{\text{TM}}$ as a function of wavelength for the chip presented in this work and (b) corresponding numerical simulations (see SM for details) (c) Measured coincidence count rate (blue squares) and CAR (green triangles) after the output microscope objective as a function of input pump power measured before the input objective. Solid lines are a guide to the eye representing a linear trend for the count rate and an inverse law for the CAR. Errorbars derived from poissonian detection statistics are smaller than symbols.

The figure of merit that we use to quantify the ability of the coupler to spatially separate the two orthogonal polarizations is the splitting ratio. For a coupling length L , it is defined for each polarization as:

$$s_{\text{TE}} \equiv \frac{P_a^{(\text{TE})}}{P_a^{(\text{TE})} + P_b^{(\text{TE})}} = \frac{1}{2} \left[1 + \cos \left(\pi \frac{L}{L_b^{(\text{TE})}} \right) \right], \quad (2)$$

$$s_{\text{TM}} \equiv \frac{P_b^{(\text{TM})}}{P_a^{(\text{TM})} + P_b^{(\text{TM})}} = \frac{1}{2} \left[1 - \cos \left(\pi \frac{L}{L_b^{(\text{TM})}} \right) \right], \quad (3)$$

where P_a^α, P_b^α is the output power at port a, b for polarization $\alpha = \text{TE}, \text{TM}$. With this definition, a perfect polarization splitting is obtained for $s_{\text{TE}} = s_{\text{TM}} = 1$ corresponding to the case where all TE-polarized light exits from arm a and all TM-polarized light exits from arm b . We perform electromagnetic simulations of the guided modes of the structure in the xz plane in the approximation of infinitely long waveguides and solve for the propagation constants $\beta_S^{\text{TE}}, \beta_{AS}^{\text{TE}}, \beta_S^{\text{TM}}, \beta_{AS}^{\text{TM}}$. We use these numerically calculated values to find the optimal (w, g) maximizing the splitting ratio over a spectral range matching the 60 nm biphoton bandwidth of the source (see Supplementary Materials for details). We simulate the propagation of light in the fundamental TE and TM modes by solving the Maxwell equations for the electric field using the numerically calculated propagation constants obtained for this set of parameters. The result of this simulation over a xy plane located in the waveguide core is shown in Fig. 1 (e). As expected, light in the TE mode exits through port a after two round trips while light in the TM mode exits through port b after one and a half round trip. To validate our design strategy, we fabricated on a single epitaxial wafer 10 devices with fixed values of waveguide width and gap and different values of coupling length L . For all these devices we measured the splitting ratio for the TE and TM fundamental modes and compared them to calculations using Eqs. (2) and (3).

The experimental characterization of the splitting ratio is done by injecting a telecom

laser beam into the generation region and recording the transmitted power at the two output ports a and b of the device as a function of the input wavelength λ . In order to access independently the TE and TM splitting ratios, the laser beam is linearly polarized either along the vertical z -axis or the horizontal x -axis (see Fig. 1 (a)). Light is coupled into the waveguide using a microscope objective (NA = 0.95) and collected simultaneously from both output arms a, b of the device using a second microscope objective (NA = 0.65) before being detected with an infrared powermeter. The chip was set at a stable temperature of 20 °C using a Peltier element in a PID loop. Fig. 2 (a) reports the experimental results obtained for the device presented in this work, and Fig. 2 (b) the corresponding numerical simulations, reproducing well the obtained results (see Supplementary Material (SM) for details about measurements and simulations on the complete set of 10 devices). All subsequent experimental measurements of this paper are acquired from this device.

On-chip generation and polarization splitting of telecom photon pairs

We assess the performance of the device in the quantum regime by generating orthogonally polarized photon pairs via SPDC in the generation region and detecting the separated photons at the two output ports of the device. To this end, we pump the input waveguide using a near-infrared CW laser (TOPTICA DL Pro 780) of 100 kHz linewidth at a wavelength of 762.5 nm using the same input and output coupling microscope objectives. Residual transmitted pump photons are filtered out using free-space long-pass filters while the generated telecom photons are fiber-coupled and detected by two superconducting nanowire single photon detectors (SNSPDs, Quantum Opus). Time-correlations between the photon detection times are recorded using a time-to-digital converter (quTools) with a 162 ps temporal

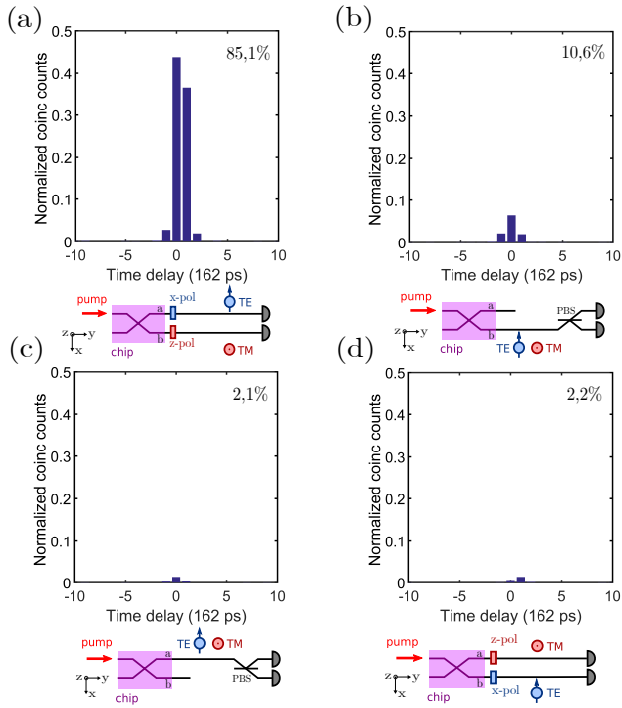


Figure 3: Measured coincidences normalized to the total number of coincidences measured in the following four configurations, showing the efficient on-chip generation and polarization splitting of the biphoton state : (a) Polarizer with transmission axis aligned along x in arm a and with transmission axis aligned along z in arm b , (b) Arm a blocked and arm b with a PBS (c) Arm b blocked and arm a with a PBS and (d) reversed configuration with respect to (a).

resolution. The measured number of coincidence counts as a function of the pump power before the input objective and corresponding coincidence-to-accidental ratio (CAR) are displayed in Fig. 2 (c). We observe that the coincidences and CAR display respectively a linear and inversely proportional dependence on the pump power as in the case of a single-waveguide AlGaAs source with off-chip pair separation.²³ The estimated collection efficiency for each arm is 11.7% and the SNSPD detection efficiency is 85%. The main limitation to the measured coincidence rate is then the propagation losses of 0.9 cm^{-1} (3.9 dB cm^{-1}) and 1.5 cm^{-1} (6.5 dB cm^{-1}) for TE and TM light respectively in the fundamental telecom mode, owing mostly to surface roughness of the waveguide and to imperfections in the materials occurring at the interface between different AlGaAs layers. The

losses can be reduced in future devices by optimizing the epitaxial structure in a design involving less AlGaAs layers as well as by improving the etching recipe of the fabrication process to obtain smoother sidewalls as demonstrated in Ref.²⁸

To certify the successful polarization splitting of the generated photon pairs, we record the number of coincidences counts in four different experimental configurations (see Fig. 3): case (a) with a linear polarizer aligned along $x(z)$ at the output of arm $a(b)$; case (b) with arm a blocked and a PBS inserted before the detectors; case (c) with arm b blocked and a PBS inserted before the detectors; case (d) with a linear polarizer aligned along $z(x)$ at the output of arm $a(b)$. The configuration of case (a) selects the events corresponding to the correct functioning of the designed polarization splitter; the configurations (b)-(d) correspond to unwanted events. The results of time correlation measurements normalized to the total number of coincidences in these four situations are reported in Fig. 3 (a)-(d). We see that the number of events measured in case a) represents 85% of the total number of emitted pairs, demonstrating the high efficiency of the polarization splitting region design. This efficiency is limited by the variation of the splitting ratio across the biphoton bandwidth, which can be reduced by the use of adiabatic couplers such as the ones described in Ref.¹⁹

Hong-Ou-Mandel interferometry at the chip output

The device operation in the quantum regime is further probed through Hong-Ou-Mandel (HOM) interference. The HOM effect, in addition to being a witness of non-classicality, represents a cornerstone of quantum information processing.²⁹ Indeed, this type of two-photon interference is widely used in quantum state engineering,^{30,31} measurement-device independent quantum key distribution³² and quantum metrology.^{33,34} Lastly, the HOM effect has been proven to be a central tool in time-frequency encoded high-dimensional quantum information

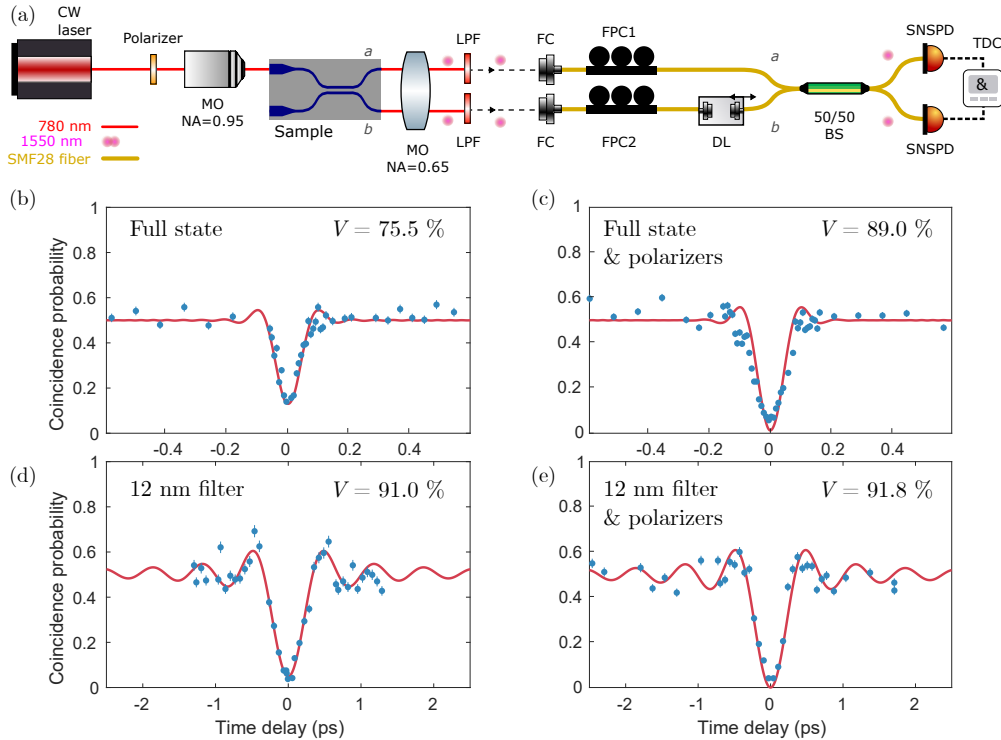


Figure 4: (a) Experimental setup for the measurement of HOM interference at the chip output. MO: Microscope objective, LPF: Low-pass frequency filter, FC: Fiber collimator, FPC: Fiber polarization controller, DL: Delay line, SNSPD: Superconducting Nanowire Single Photon Detector, TDC: Time-to-digital converter. (b-c) Unfiltered HOM interferograms obtained (b) without and (c) with polarizers at the output of the device (see main text for details). (d-e) HOM interferograms with 12 nm spectral filter obtained (d) without and (e) with polarizers at the output of the device. Error bars are calculated assuming Poissonian statistics.

with biphoton states.^{25,35}

The experimental setup used to perform HOM interference at the output of the device is depicted in Fig. 4 (a). Input and output coupling are done with the same microscope objectives used in the previous experiment. After pump filtering and fiber collimation, we apply a temporal delay on arm *b* using a free-space delay line before recombining the two photons on a fiber 50/50 beam splitter (BS) and detecting them at the output of the BS with SNSPDs. The two fiber polarization controllers (FPC) are used to ensure that the polarization of the two photons is identical in the fiber interferometer.

To probe separately the impact of the properties of the generated quantum state and of the polarization splitting ratio of the device on the two-photon interference, we measure the HOM interferogram in four different settings: first, using the full generated state respectively with-

out and with the addition of polarizers at the chip output; then in the same measurements settings but using the generated quantum state spectrally filtered around degeneracy with a 12 nm-wide filter.

In Fig. 4 (b) we plot the result of a HOM measurement taken directly at the chip output without any spectral filtering nor added polarizers. The measured visibility, given by $V = (C_{\text{ref}} - C_{\text{min}})/C_{\text{ref}}$,²⁹ where C_{ref} is the coincidence reference level taken at large temporal delay and C_{min} is the coincidence minimum, is $75.5\% \pm 5.4\%$ exceeding the classical threshold of 50% thus showing that the integrated source and splitter operate in the quantum regime. We stress that all the visibility values given in this work are raw, meaning that the noise counts are not subtracted. The red curve corresponds to the calculated HOM coincidence probability obtained from the simulated quantum state

produced in the generation region and the experimentally measured splitting ratios s_{TE} , s_{TM} (see Supplementary Materials for details). We observe that the agreement between our model and the experimental results is excellent.

In Fig. 4 (c) we plot the results obtained by inserting in each optical paths a and b a linear polarizer with transmission axis respectively aligned along the x and z -direction. The obtained visibility in this case is $V = 89\% \pm 4.6\%$, a value which is in agreement with previous experiments on AlGaAs sources consisting of a single straight ridge waveguide followed by an off-chip fiber polarizing beam splitter,^{24,25} supporting the idea that this measurement gives access to the intrinsic visibility of the generated two-photon state. The limitation to this value comes from waveguide birefringence causing spectral asymmetry with respect to frequency degeneracy between TE and TM-polarized photons. As a result, our measurement shows that a perfect splitting ratio over the whole state bandwidth would allow to reach the maximum value of visibility allowed by the source properties.

We emphasize that both HOM interferograms were obtained with a broadband biphoton state as opposed to previous demonstrations reported in periodically poled lithium niobate (ppLN) where off-chip filters were used¹³ or in Silicon chips generating narrowband degenerate photon pairs.³⁶ The width of the experimentally measured HOM dip in Fig. 4 (b-c) is approximately 90 fs, corresponding to a two-photon bandwidth of 63 nm comparable to the expected 60 nm reported in Ref.,²⁶ indicating the broadband character of the measured quantum state. To quantify the effect of spectral filtering on the performances of our device, we repeat the HOM measurement after adding at the chip output a 12 nm filter centered on the biphoton degeneracy frequency. We obtain a value of $V = 91.0\% \pm 6.6\%$ without polarizers (Fig. 4 (d)) and $V = 91.8\% \pm 6.9\%$ with polarizers (Fig. 4 (e)). The improvement in HOM visibility when adding polarizers is negligible here since the splitting ratio stays very high in this 12 nm bandwidth as shown in Fig. 2 (a). This value is of the same order as in previous

state-of-the-art realizations in other platforms, but we notice that in our case the available spectral bandwidth is one order of magnitude higher (1.2 nm in¹³). We stress the relevance of this result by pointing out that spectral filtering is commonly used in many applications such as wavelength-multiplexed quantum communications²⁶ or frequency-based quantum information³⁷ where the emitted photons have to be divided into spectral bins by the use of filters. Hence, in most cases, the spectral asymmetry with respect to frequency degeneracy between the two photons of the pairs causing imperfect HOM visibility is naturally suppressed by the action of filtering.

Conclusion and outlook

In summary, we have demonstrated a monolithic nonlinear AlGaAs waveguide circuit integrating the generation of spectrally broadband photon pairs in the telecom range and their polarization splitting with a birefringent directional coupler. By precise engineering of the waveguide birefringence and phase-matching wavelengths, the challenging task of combining these two functionalities in a simple device made by a one-step etching process has been fulfilled. 85% of the pairs are deterministically separated by the chip over a 60 nm bandwidth. Its performances in the quantum regime have been assessed via a Hong-Ou-Mandel interference experiment displaying a visibility of 75.5% (91%) for a 60 nm (12 nm) broad biphoton state. We notice that a maximal visibility of the HOM dip requires that the splitting ratio curves for the TE and TM modes are superposed and symmetric with respect to the frequency degeneracy for the down-conversion process; a possible way to improve the performances of the present device is to adjust the waveguide width of the generation region to shift the frequency degeneracy of the generated state at the optimal wavelength. Further progress on the device performances is possible following two main directions: on one hand the design of the epitaxial structure could be optimized in order to reduce the modal birefrin-

gence thus increasing the HOM visibility.³⁸ On the other hand, the design of the polarization splitting region could be refined by using adiabatic couplers which, in LN waveguides without an on-chip photon pair source, have been shown to exhibit a flat spectral profile with splitting ratios above 98 % over a spectral range of more than 100 nm.¹⁹ Another interesting approach could be the use of inverse design³⁹ to improve the figure-of-merit for the directional coupler, as done for example in Ref.⁴⁰ In any case, the device presented in this work can already be used as a source of broadband frequency anticorrelated photon pairs separated in two different spatial modes, directly employable for information processing protocols based on high-dimensional quantum states.^{41,42} Using both input arms of the splitting region to generate orthogonally polarized photon pairs would also allow to obtain a source of polarization entangled photon pairs directly separated in two spatial modes, as reported in ppLN¹², albeit with a narrow bandwidth (0.25 nm) in the latter work. Using AlGaAs would not only allow a miniaturization of the device of around one order of magnitude, but also to take benefit of the low modal birefringence to avoid temporal walk-off post-compensation in frequency channel-based quantum networks. By taking a step further the device could be upgraded by adding an electro-optic delay line,²⁰ a polarization rotator⁴³ and a 50/50 mode splitter.⁴⁴ In this configuration the photons, after being generated in a waveguide, would be deterministically separated at the polarizing mode splitter and time-shifted by the electro-optic delay line; one of them could be polarization rotated and finally the two photons would be recombined on the 50/50 mode splitter. Such nonlinear integrated quantum electro-optic circuit would enable a full flexible control over single-qubit operations¹³ as well as an on-chip generation of polarization-frequency hyperentangled states⁴⁵ over a wide spectral range, opening promising perspectives for its utilization in quantum communication networks.⁴⁶

Note: The authors declare no conflicts of interest.

Acknowledgement This work was supported by Defence Innovation Agency under grant ANR-19-ASTR- **0018 01**), the French RENATECH network, and by Paris Ile-de-France Region in the framework of DIM SIRTEQ through the Project Paris QCI and Project LION. The authors also acknowledge partial funding from the French government through the National Research Agency (ANR) in the context of the Plan France 2030 through project reference ANR-22-PETQ-0011. O.M. acknowledges Labex SEAM (Science and Engineering for Advanced Materials and devices), ANR-10-LABX-0096 and ANR-18-IDEX-0001 for financial support.

Supporting Information Available

- See Supplemental Material for supporting content on device fabrication, electromagnetic simulation of the splitting region and calculation of the HOM coincidence probability.
- Data underlying the results presented in this paper are not publicly available at this time but may be obtained from the authors upon reasonable request.

References

- (1) Flamini, F.; Spagnolo, N.; Sciarrino, F. Photonic quantum information processing: a review. *Reports on Progress in Physics* **2018**, *82*, 016001.
- (2) Polino, E.; Valeri, M.; Spagnolo, N.; Sciarrino, F. Photonic quantum metrology. *AVS Quantum Sci.* **2020**, *2*, 024703.
- (3) Han-Sen, Z. et al. Quantum computational advantage using photons. *Science* **2020**, *370*, 1460–1463.
- (4) Madsen, L. S. et al. Quantum computational advantage with a programmable

- photonic processor. *Nature* **2022**, *606*, 75–81, Number: 7912 Publisher: Nature Publishing Group.
- (5) Tse, M. et al. Quantum-Enhanced Advanced LIGO Detectors in the Era of Gravitational-Wave Astronomy. *PRL* **2019**, *123*, 231107.
 - (6) Collaboration, V. et al. Increasing the Astrophysical Reach of the Advanced Virgo Detector via the Application of Squeezed Vacuum States of Light. *PRL* **2019**, *123*, 231108.
 - (7) Wang, J.; Sciarrino, F.; Laing, A.; Thompson, M. G. Integrated photonic quantum technologies. *Nature Photonics* **2020**, *14*, 273–284.
 - (8) Pelucchi, E. et al. The potential and global outlook of integrated photonics for quantum technologies. *Nature Reviews Physics* **2022**, *4*, 194–208.
 - (9) Adcock, J. C.; Bao, J.; Chi, Y.; Chen, X.; Bacco, D.; Gong, Q.; Oxenløwe, L. K.; Wang, J.; Ding, Y. Advances in Silicon Quantum Photonics. *IEEE Journal of Selected Topics in Quantum Electronics* **2021**, *27*, 1–24.
 - (10) Mondain, F.; Lunghi, T.; Zavatta, A.; Gouzien, E.; Dautre, F.; Micheli, M. D.; Tanzilli, S.; D’Auria, V. Chip-based squeezing at a telecom wavelength. *Photon. Res.* **2019**, *7*, A36–A39.
 - (11) Nehra, R.; Sekine, R.; Ledezma, L.; Guo, Q.; Gray, R. M.; Roy, A.; Marandi, A. Few-cycle vacuum squeezing in nanophotonics. *Science* **2022**, *377*, 1333–1337.
 - (12) Sansoni, L.; Luo, K. H.; Eigner, C.; Ricken, R.; Quiring, V.; Herrmann, H.; Silberhorn, C. A two-channel, spectrally degenerate polarization entangled source on chip. *npj Quantum Information* **2017**, *3*, 5.
 - (13) Luo, K.-H.; Brauner, S.; Eigner, C.; Sharapova, P. R.; Ricken, R.; Meier, T.; Herrmann, H.; Silberhorn, C. Nonlinear integrated quantum electro-optic circuits. *Sci. Adv.* **2019**, *5*, eaat1451.
 - (14) Kues, M.; Reimer, C.; Lukens, J. M.; Munro, W. J.; Weiner, A. M.; Moss, D. J.; Morandotti, R. Quantum optical microcombs. *Nature Photonics* **2019**, *13*, 170–179.
 - (15) Wu, H.; Tan, Y.; Dai, D. Ultra-broadband high-performance polarizing beam splitter on silicon. *Opt. Express* **2017**, *25*, 6069–6075.
 - (16) Xu, H.; Dai, D.; Shi, Y. Ultra-Broadband and Ultra-Compact On-Chip Silicon Polarization Beam Splitter by Using Hetero-Anisotropic Metamaterials. *Laser & Photonics Reviews* **2019**, *13*, 1800349.
 - (17) Guerber, S.; Alonso-Ramos, C.; Benedikovic, D.; Durán-Valdeiglesias, E.; Roux, X. L.; Vulliet, N.; Cassan, E.; Marris-Morini, D.; Baudot, C.; Boeuf, F.; Vivien, L. Broadband Polarization Beam Splitter on a Silicon Nitride Platform for O-Band Operation. *IEEE Photonics Technology Letters* **2018**, *30*, 1679–1682.
 - (18) Huang, G.; Park, T.-H.; Oh, M.-C. Broadband integrated optic polarization splitters by incorporating polarization mode extracting waveguide. *Scientific Reports* **2017**, *7*, 4789.
 - (19) Chung, H.-P.; Lee, C.-H.; Huang, K.-H.; Yang, S.-L.; Wang, K.; Solntsev, A. S.; Sukhorukov, A. A.; Setzpfandt, F.; Chen, Y.-H. Broadband on-chip polarization mode splitters in lithium niobate integrated adiabatic couplers. *Opt. Express* **2019**, *27*, 1632.
 - (20) Wang, J. et al. Gallium arsenide (GaAs) quantum photonic waveguide circuits. *Optics Communications* **2014**, *327*, 49–55.
 - (21) Boitier, F.; Orioux, A.; Autebert, C.; Lemaître, A.; Galopin, E.; Manquest, C.;

- Sirtori, C.; Favero, I.; Leo, G.; Ducci, S. Electrically Injected Photon-Pair Source at Room Temperature. *Phys. Rev. Lett.* **2014**, *112*.
- (22) Appas, F.; Meskine, O.; Lemaître, A.; Morassi, M.; Baboux, F.; Amanti, M. I.; Ducci, S. Nonlinear Quantum Photonics With AlGaAs Bragg-Reflection Waveguides. *Journal of Lightwave Technology* **2022**, 1–11.
- (23) Horn, R.; Abolghasem, P.; Bijlani, B. J.; Kang, D.; Helmy, A. S.; Weihs, G. Monolithic Source of Photon Pairs. *Phys. Rev. Lett.* **2012**, *108*.
- (24) Autebert, C.; Bruno, N.; Martin, A.; Lemaître, A.; Carbonell, C. G.; Favero, I.; Leo, G.; Zbinden, H.; Ducci, S. Integrated AlGaAs source of highly indistinguishable and energy-time entangled photons. *Optica* **2016**, *3*, 143.
- (25) Maltese, G.; Amanti, M. I.; Appas, F.; Sinnl, G.; Lemaître, A.; Milman, P.; Baboux, F.; Ducci, S. Generation and symmetry control of quantum frequency combs. *npj Quantum Inf.* **2020**, *6*, 13.
- (26) Appas, F.; Baboux, F.; Amanti, M. I.; Lemaître, A.; Boitier, F.; Diamanti, E.; Ducci, S. Flexible entanglement-distribution network with an AlGaAs chip for secure communications. *npj Quantum Inf.* **2021**, *7*, 117.
- (27) Yariv, A.; Yeh, P. *Photonics*; Oxford University Press Inc, 2006; pp 611–618.
- (28) Chang, L.; Xie, W.; Shu, H.; Yang, Q.-F.; Shen, B.; Boes, A.; Peters, J. D.; Jin, W.; Xiang, C.; Liu, S.; et al., Ultra-efficient frequency comb generation in AlGaAs-On-Insulator microresonators. *Nature Communications* **2020**, *11*, 1331.
- (29) Bouchard, F.; Sit, A.; Zhang, Y.; Fickler, R.; Miatto, F. M.; Yao, Y.; Sciarino, F.; Karimi, E. Two-photon interference: the Hong–Ou–Mandel effect. *Reports on Progress in Physics* **2021**, *84*, 012402.
- (30) Chen, Y.; Ecker, S.; Wengerowsky, S.; Bulla, L.; Joshi, S. K.; Steinlechner, F.; Ursin, R. Polarization Entanglement by Time-Reversed Hong-Ou-Mandel Interference. *Phys. Rev. Lett.* **2018**, *121*, 200502.
- (31) Francesconi, S.; Baboux, F.; Raymond, A.; Fabre, N.; Boucher, G.; Lemaître, A.; Milman, P.; Amanti, M. I.; Ducci, S. Engineering two-photon wavefunction and exchange statistics in a semiconductor chip. *Optica* **2020**, *7*, 316.
- (32) Lo, H.-K.; Curty, M.; Qi, B. Measurement-Device-Independent Quantum Key Distribution. *Phys. Rev. Lett.* **2012**, *108*, 130503.
- (33) Hong, C. K.; Ou, Z. Y.; Mandel, L. Measurement of subpicosecond time intervals between two photons by interference. *Phys. Rev. Lett.* **1987**, *59*, 2044–2046.
- (34) Lyons, A.; Knee, G. C.; Bolduc, E.; Roger, T.; Leach, J.; Gauger, E. M.; Faccio, D. Attosecond-resolution Hong-Ou-Mandel interferometry. *Science Advances* **2018**, *4*, eaap9416.
- (35) Fabre, N.; Maltese, G.; Appas, F.; Felicetti, S.; Ketterer, A.; Keller, A.; Coudreau, T.; Baboux, F.; Amanti, M. I.; Ducci, S.; Milman, P. Generation of a time-frequency grid state with integrated biphoton frequency combs. *Phys. Rev. A* **2020**, *102*, 012607.
- (36) He, J.; Bell, B. A.; Casas-Bedoya, A.; Zhang, Y.; Clark, A. S.; Xiong, C.; Eggleton, B. J. Ultracompact quantum splitter of degenerate photon pairs. *Optica* **2015**, *2*, 779–782.
- (37) Kues, M.; Reimer, C.; Roztocki, P.; Cortés, L. R.; Sciara, S.; Wetzel, B.; Zhang, Y.; Cino, A.; Chu, S. T.; Little, B. E.; Moss, D. J.; Caspani, L.

- Azaña, J.; Morandotti, R. On-chip generation of high-dimensional entangled quantum states and their coherent control. *Nature* **2017**, *546*, 622–626.
- (38) Chen, H.; Laiho, K.; Pressl, B.; Schlager, A.; Suchomel, H.; Kamp, M.; Höfling, S.; Schneider, C.; Weihs, G. Optimizing the spectro-temporal properties of photon pairs from Bragg-reflection waveguides. *Journal of Optics* **2019**, *21*, 054001.
- (39) Molesky, S.; Lin, Z.; Piggott, A. Y.; Jin, W.; Vucković, J.; Rodriguez, A. W. Inverse design in nanophotonics. *Nature Photonics* **2018**, *12*, 659–670.
- (40) Frandsen, L. H.; Sigmund, O. Inverse design engineering of all-silicon polarization beam splitters. Photonic and Phononic Properties of Engineered Nanostructures VI. 2016; p 97560Y.
- (41) Imany, P.; Jaramillo-Villegas, J. A.; Alshaykh, M. S.; Lukens, J. M.; Odele, O. D.; Moore, A. J.; Leaird, D. E.; Qi, M.; Weiner, A. M. High-dimensional optical quantum logic in large operational spaces. *npj Quantum Information* **2019**, *5*, 59.
- (42) Lu, H.-H.; Lukens, J. M.; Williams, B. P.; Imany, P.; Peters, N. A.; Weiner, A. M.; Loughovski, P. A controlled-NOT gate for frequency-bin qubits. *npj Quantum Information* **2019**, *5*, 24.
- (43) Huan, Z.; Scarmozzino, R.; Nagy, G.; Steel, J.; Osgood, R. Realization of a compact and single-mode optical passive polarization converter. *IEEE Photonics Technology Letters* **2000**, *12*, 317–319.
- (44) Belhassen, J.; Baboux, F.; Yao, Q.; Amanti, M.; Favero, I.; Lemaitre, A.; Kolthammer, W. S.; Walmsley, I. A.; Ducci, S. On-chip III-V monolithic integration of heralded single photon sources and beamsplitters. *Appl. Phys. Lett.* **2018**, *112*, 071105.
- (45) Xie, Z.; Zhong, T.; Shrestha, S.; Xu, X.; Liang, J.; Gong, Y.-X.; Bienfang, J. C.; Restelli, A.; Shapiro, J. H.; Wong, F. N. C.; Wei Wong, C. Harnessing high-dimensional hyperentanglement through a biphoton frequency comb. *Nature Photonics* **2015**, *9*, 536–542.
- (46) Graham, T. M.; Bernstein, H. J.; Wei, T.-C.; Junge, M.; Kwiat, P. G. Superdense teleportation using hyperentangled photons. *Nature Communications* **2015**, *6*, 7185.

Supplementary Material: Broadband biphoton generation and polarization splitting in a monolithic AlGaAs chip

Félicien Appas,^{†,‡,||} Othmane Meskine,^{†,||} Aristide Lemaître,[¶] José Palomo,[§]
 Florent Baboux,[†] Maria I. Amanti,^{*,†} and Sara Ducci^{*,†}

[†]*Université Paris Cité, CNRS, Laboratoire Matériaux et Phénomènes Quantiques, 75013 Paris, France*

[‡]*Current address: ICFO - Institut de Ciències Fotoniques, The Barcelona Institute of Science and Technology, Castelldefels (Barcelona) 08860, Spain*

[¶]*Université Paris-Saclay, CNRS, Centre de Nanosciences et de Nanotechnologies, 91120, Palaiseau, France*

[§]*Laboratoire de Physique de l'École normale supérieure, ENS, Université PSL, CNRS, Sorbonne Université, Université Paris Cité, F-75005 Paris, France*

^{||}*These authors contributed equally to this work*

E-mail: maria.amanti@u-paris.fr; sara.ducci@u-paris.fr

Methods

Device epitaxial structure and fabrication

The photonic chip is fabricated out of an epitaxially-grown AlGaAs wafer consisting of a 6-period $\text{Al}_{0.80}\text{Ga}_{0.20}\text{As}/\text{Al}_{0.25}\text{Ga}_{0.75}\text{As}$ Bragg reflector (lower mirror), a 351 nm $\text{Al}_{0.45}\text{Ga}_{0.55}\text{As}$

core and a 2-period $\text{Al}_{0.25}\text{Ga}_{0.75}\text{As}/\text{Al}_{0.80}\text{Ga}_{0.20}\text{As}$ Bragg reflector (upper mirror) grown on a GaAs wafer. The structure is designed such that the dispersion of the guided modes allows for Type II modal phase-matching between the so-called near-infrared TE Bragg mode at and the telecom TE and TM fundamental modes enabling the generation of cross-polarized photon pairs through Type II SPDC.¹ Only the first four upper layers, corresponding to the upper Bragg mirror, are etched resulting in a ridge height of around 800 nm. The core layer is not etched to ensure optimal coupling between the propagating modes of the waveguides in the evanescent coupling region. Indeed, if the core is etched, then the overlap between the spatial profile of the fundamental modes $\mathbf{E}_a, \mathbf{E}_b$ is drastically reduced, thus increasing the optimal coupling length and the subsequent device footprint.

The chip is fabricated using electron-beam lithography on a 6% silsesquioxane-based H-SiOx (HSQ) resist and Cl-based ICP etching. After fabrication, the sample is cleaved mechanically along the $[1\bar{1}0]$ crystallographic axis to obtain optical quality facets. The final overall chip length, including the source and the polarization splitter, is 7 mm. The output waveguide spacing is 127 μm , corresponding to a standard fiber array pitch.

Electromagnetic simulation of the device splitting ratio

We perform electromagnetic mode analysis in our integrated polarization mode splitter design using commercially available software suite to find a region in parameter space where condition $L_c^{(\text{TE})}/L_c^{(\text{TM})} = 3/4$ is fulfilled. Maxwell's equations in the coupled waveguide structure are solved using finite element methods to obtain the spatial xz profile and effective index of a given number of modes at a fixed frequency. We implemented a simple algorithm to automatically detect the two S and AS supermodes from the multitude of guided modes that are calculated.

From the simulated effective S and AS mode indices, we were able to compute the transmitted power for both polarizations as a function of the waveguide width w_{sim} , gap g_{sim} and coupling length L_{sim} and infer the TE and TM splitting ratio as shown in Fig. S1 (a-b).

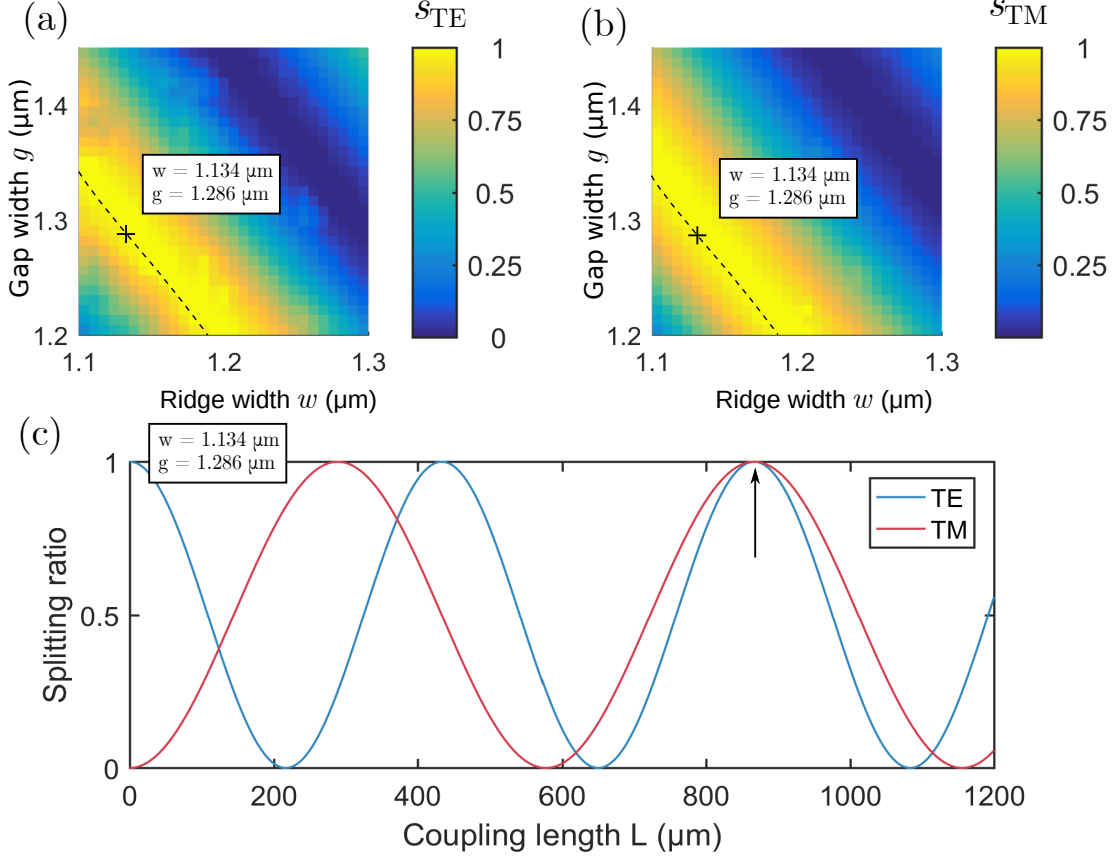


Figure S1: (a) TE and (b) TM splitting ratio as a function of waveguide width w_{sim} and gap g_{sim} for a coupling length of $L_{\text{sim}} = 864 \mu\text{m}$ and at a wavelength $\lambda = 1525 \text{ nm}$. (c) Splitting ratio as a function of coupling length L for the set of parameters $w_{\text{sim}} = 1.134 \mu\text{m}$, $g_{\text{sim}} = 1.286 \mu\text{m}$ and $\lambda = 1525 \text{ nm}$. The optimal working point, for which $s_{TE} = s_{TM} = 1$, is indicated by an arrow.

At a wavelength of 1525 nm , for $L_{\text{sim}} = 864 \mu\text{m}$, we observe that the dotted lines denoting the regions where s_{TE} and s_{TM} are equal to 1 can be almost perfectly superimposed. As a consequence, in this design, we can achieve simultaneously perfect TE and TM polarization splitting. The optimal working point, corresponding to the region where the two TE and TM dotted lines have the best overlap, is denoted by a cross. This corresponds to a situation where $L_c^{(TE)}/L_c^{(TM)} = 3/4$. In Fig.S1 (c), we plot the TE and TM splitting ratios as a function of coupling length for the optimal set of parameters $w_{\text{sim}} = 1.134 \mu\text{m}$, $g_{\text{sim}} = 1.286 \mu\text{m}$. The two oscillating curves correspond to the beating of the cosine terms in Eq. (2-3) of the main text and the optimal coupling length $L_{\text{sim}} = 864 \mu\text{m}$ at $\lambda = 1525 \text{ nm}$ is indicated by a black

arrow.

Dependence of the splitting ratio on the coupling length

L

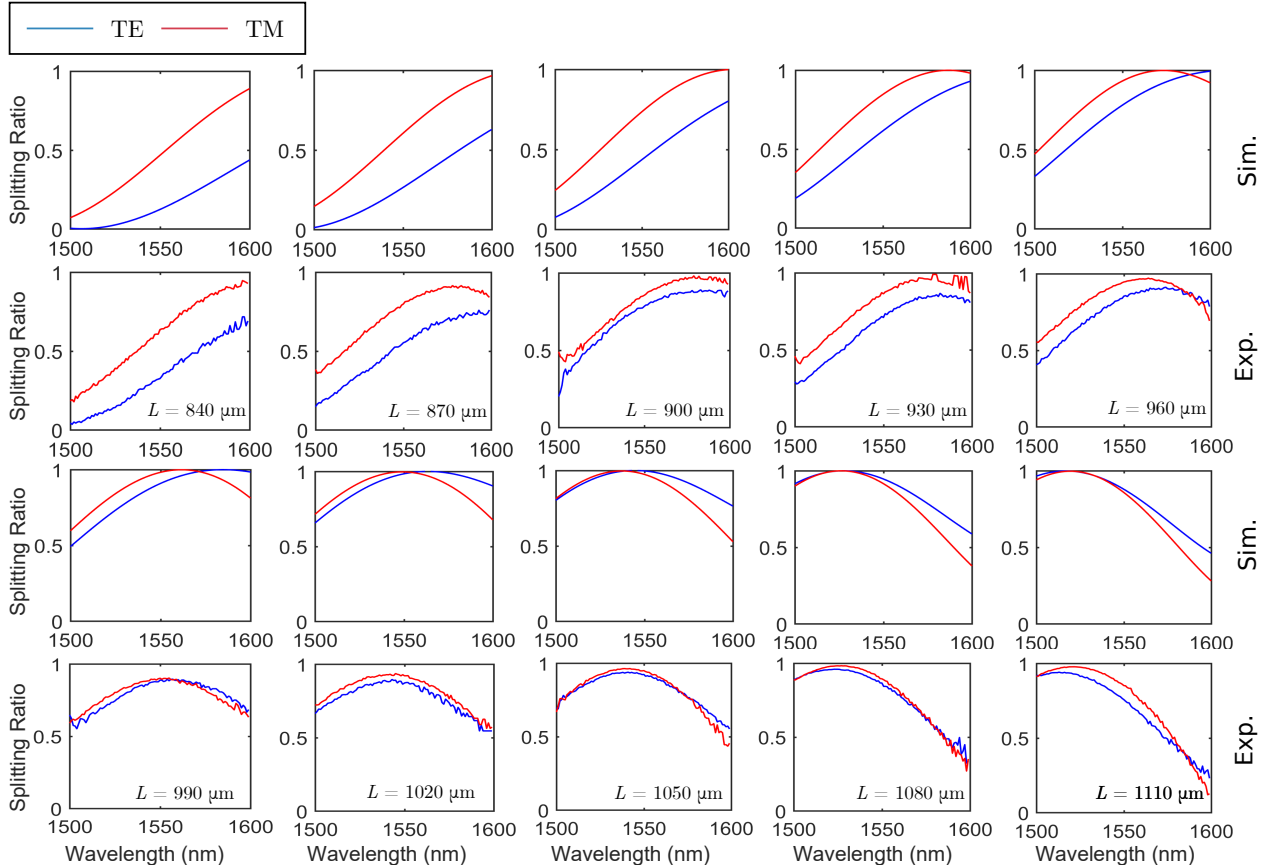


Figure S2: Simulated and measured TE and TM splitting ratios as a function of wavelength for different values of the coupling length L in a device with $w = 1.29 \mu\text{m}$ and $g = 1.51 \mu\text{m}$.

The length of the straight portion of the directional coupler provides a useful tuning parameter to adjust the splitting ratio to the biphoton degeneracy frequency. In Fig. S2 we present the measured and calculated splitting ratios for different device lengths. As can be seen the maxima of the TE and TM splitting ratios can be blue or red-shifted by decreasing or increasing L . The corresponding simulations were obtained with the set of parameters $w_{\text{sim}} = 1.134 \mu\text{m}$, $g_{\text{sim}} = 1.286 \mu\text{m}$ and $L_{\text{sim}} = \gamma L$ where $\gamma = 0.8$ is a scaling factor that

accounts for the effect of imperfect epitaxial structure on propagation. The experimentally measured TE and TM splitting ratios for different values of the coupling length L correspond to a device with $w = 1.29 \mu\text{m}$ and $g = 1.51 \mu\text{m}$.

Calculation of the Hong-Ou-Mandel coincidence probability

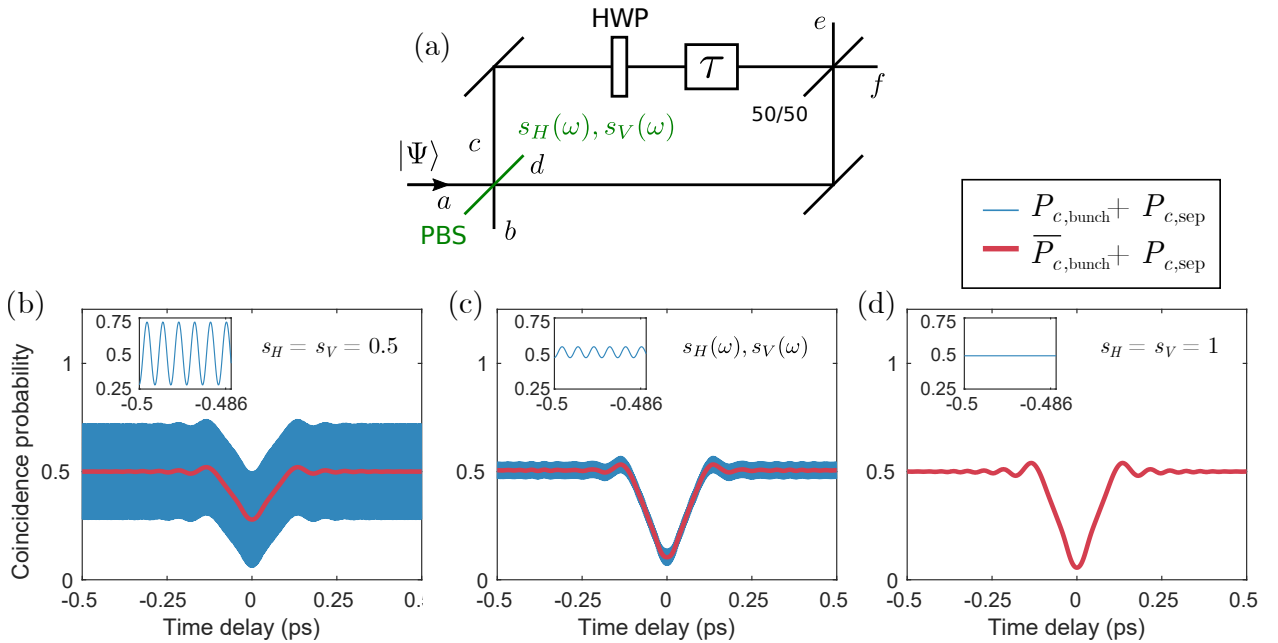


Figure S3: (a) Scheme modelling a Hong-Ou-Mandel interference with a frequency-dependent polarizing beam splitter. HWP: Half-wave plate, PBS: Polarizing beam splitter. (b-d) Simulated HOM coincidence probability P_c showing different contributions from the terms $P_{c,\text{sep}}$ and $P_{c,\text{bunch}}$ for different values of the PBS splitting ratio: (b) $s_H = s_V = 0.5$, (c) $s_H(\omega), s_V(\omega)$ given by the experimental values of the device of coupling length $L = 1080 \mu\text{m}$ (d) $s_H = s_V = 1$. The inset displays the value of P_c over a 14 fs window at $\tau = -0.5 \text{ ps}$ showing the oscillations originating from the term $P_{c,\text{bunch}}$.

To model Hong-Ou-Mandel (HOM) effect in our integrated device, we use the physical picture sketched in Fig. S3 (a). The photon pairs emitted by the source are incident on a frequency-dependent polarizing beam splitter, which models the polarization splitting region of our device. We assume that the two photons are initially in the same arm a of the PBS.

Then, after they exit the PBS, a delay is applied to arm c and the polarization in this arm is rotated with a half-wave plate such that the two photons end up with identical polarization. As in a usual HOM interferometer, the photons are recombined on a 50/50 beam splitter. The goal here is to calculate the coincidence probability between the output arms e, f of the 50/50 beam splitter. We start from the generated SPDC state of our source:²

$$|\Psi\rangle = \iint d\omega_1 d\omega_2 \mathcal{C}(\omega_1, \omega_2) |\omega_1, H, a\rangle |\omega_2, V, a\rangle, \quad (1)$$

where $|\omega, H, a\rangle = \hat{a}_H^\dagger(\omega) |\text{vac}\rangle$, $|\omega, V, a\rangle = \hat{a}_V^\dagger(\omega) |\text{vac}\rangle$ and $\mathcal{C}(\omega_1, \omega_2)$ the joint spectral amplitude (JSA) is assumed to be normalized $\iint d\omega_1 d\omega_2 |\mathcal{C}(\omega_1, \omega_2)|^2 = 1$. Here, the labels H, V denote TE and TM modes respectively. The action of the frequency-dependent PBS is represented by a unitary transformation acting separately on the H and V subspaces:

$$\hat{a}_H(\omega) = \sqrt{s_H(\omega)} \hat{c}_H(\omega) + \sqrt{1 - s_H(\omega)} \hat{d}_H(\omega), \quad (2)$$

$$\hat{b}_H(\omega) = \sqrt{1 - s_H(\omega)} \hat{c}_H(\omega) - \sqrt{s_H(\omega)} \hat{d}_H(\omega), \quad (3)$$

$$\hat{a}_V(\omega) = \sqrt{1 - s_V(\omega)} \hat{c}_V(\omega) + \sqrt{s_V(\omega)} \hat{d}_V(\omega), \quad (4)$$

$$\hat{b}_V(\omega) = \sqrt{s_V(\omega)} \hat{c}_V(\omega) - \sqrt{1 - s_V(\omega)} \hat{d}_V(\omega), \quad (5)$$

where the coefficients $s_H(\omega), s_V(\omega)$ are the TE and TM splitting ratios of the polarization splitter. After the PBS, the quantum state evolves into $|\Psi\rangle = |\Psi\rangle_{\text{sep}} + |\Psi\rangle_{\text{bunch}}$ where the two independent contribution are:

$$|\Psi\rangle_{\text{sep}} = \iint d\omega_1 d\omega_2 \mathcal{C}(\omega_1, \omega_2) |\omega_1, H\rangle |\omega_2, V\rangle \left(\sqrt{s_H(\omega_1)} \sqrt{s_V(\omega_2)} |c\rangle |d\rangle \right. \\ \left. + \sqrt{1 - s_H(\omega_1)} \sqrt{1 - s_V(\omega_2)} |d\rangle |c\rangle \right), \quad (6)$$

$$|\Psi\rangle_{\text{bunch}} = \iint d\omega_1 d\omega_2 \mathcal{C}(\omega_1, \omega_2) |\omega_1, H\rangle |\omega_2, V\rangle \left(\sqrt{s_H(\omega_1)} \sqrt{1 - s_V(\omega_2)} |c\rangle |c\rangle \right. \\ \left. + \sqrt{1 - s_H(\omega_1)} \sqrt{s_V(\omega_2)} |d\rangle |d\rangle \right). \quad (7)$$

These terms describe the two distinct cases where the two photons are either separated into distinct paths $|\Psi\rangle_{\text{sep}}$ or end up into the same spatial mode $|\Psi\rangle_{\text{bunch}}$. After being transformed by the delay line and HWP, the state reads:

$$|\Psi\rangle_{\text{sep}} = \iint d\omega_1 d\omega_2 \mathcal{C}(\omega_1, \omega_2) |\omega_1, V, c\rangle |\omega_2, V, d\rangle \sqrt{s_H(\omega_1)} \sqrt{s_V(\omega_2)} e^{-i\omega_1 \tau} \quad (8)$$

$$+ \iint d\omega_1 d\omega_2 \mathcal{C}(\omega_1, \omega_2) |\omega_1, H, d\rangle |\omega_2, H, c\rangle \sqrt{1-s_H(\omega_1)} \sqrt{1-s_V(\omega_2)} e^{-i\omega_2 \tau},$$

$$|\Psi\rangle_{\text{bunch}} = \iint d\omega_1 d\omega_2 \mathcal{C}(\omega_1, \omega_2) |\omega_1, V, c\rangle |\omega_2, H, c\rangle \sqrt{s_H(\omega_1)} \sqrt{1-s_V(\omega_2)} e^{-i(\omega_1+\omega_2)\tau}$$

$$+ \iint d\omega_1 d\omega_2 \mathcal{C}(\omega_1, \omega_2) |\omega_1, H, d\rangle |\omega_2, V, d\rangle \sqrt{1-s_H(\omega_1)} \sqrt{s_V(\omega_2)}. \quad (9)$$

Then the two photons enter the 50/50 beam splitter whose action can be modeled by the usual unitary transform: $|c\rangle = (|e\rangle + |f\rangle)/\sqrt{2}$, $|d\rangle = (|e\rangle - |f\rangle)/\sqrt{2}$. We post-select the states where both photons exit through opposite output ports and, after grouping the different terms, we obtain the following expression:

$$|\Psi'\rangle_{\text{sep}} = \frac{1}{2} \iint d\omega_1 d\omega_2 \left(\mathcal{C}(\omega_1, \omega_2) \sqrt{s_H(\omega_1)} \sqrt{s_V(\omega_2)} e^{-i\omega_1 \tau} \right. \\ \left. - \mathcal{C}(\omega_2, \omega_1) \sqrt{s_H(\omega_2)} \sqrt{s_V(\omega_1)} e^{-i\omega_2 \tau} \right) |\omega_1, V, e\rangle |\omega_2, V, f\rangle \quad (10)$$

$$+ \frac{1}{2} \iint d\omega_1 d\omega_2 \left(\mathcal{C}(\omega_1, \omega_2) \sqrt{1-s_H(\omega_1)} \sqrt{1-s_V(\omega_2)} e^{-i\omega_1 \tau} \right. \\ \left. - \mathcal{C}(\omega_2, \omega_1) \sqrt{1-s_H(\omega_2)} \sqrt{1-s_V(\omega_1)} e^{-i\omega_2 \tau} \right) |\omega_1, H, e\rangle |\omega_2, H, f\rangle,$$

$$|\Psi'\rangle_{\text{bunch}} = \frac{1}{2} \iint d\omega_1 d\omega_2 \left(\mathcal{C}(\omega_1, \omega_2) \sqrt{s_H(\omega_1)} \sqrt{1-s_V(\omega_2)} e^{-i(\omega_1+\omega_2)\tau} \right. \\ \left. - \mathcal{C}(\omega_2, \omega_1) \sqrt{1-s_H(\omega_2)} \sqrt{s_V(\omega_1)} \right) |\omega_1, V, e\rangle |\omega_2, H, f\rangle \quad (11)$$

$$+ \frac{1}{2} \iint d\omega_1 d\omega_2 \left(\mathcal{C}(\omega_1, \omega_2) \sqrt{s_H(\omega_1)} \sqrt{1-s_V(\omega_2)} e^{-i(\omega_1+\omega_2)\tau} \right. \\ \left. - \mathcal{C}(\omega_2, \omega_1) \sqrt{1-s_H(\omega_2)} \sqrt{s_V(\omega_1)} \right) |\omega_1, H, e\rangle |\omega_2, V, f\rangle.$$

As we can see from Eqs. (10) and (11), the coincidence probability will be the sum of four terms corresponding to the four possible output polarization states : VV, HH, VH, HV ,

in other words: $P_c = P_{c,\text{sep}} + P_{c,\text{bunch}} = P_{VV} + P_{HH} + P_{VH} + P_{HV}$. The four terms can be calculated individually using the suitable projection operators:³

$$P_{\mu\nu} = \langle \Psi | \left(\int d\omega |\omega, \mu, e\rangle \langle \omega, \mu, e| \right) \left(\int d\omega' |\omega', \nu, f\rangle \langle \omega', \nu, f| \right) | \Psi \rangle, \quad (12)$$

with $\mu, \nu = H, V$. We obtain the following coincidence probabilities:

$$\begin{aligned} P_{c,\text{sep}} &= P_{VV} + P_{HH} \\ &= \frac{1}{4} \iint d\omega_1 d\omega_2 |\mathcal{C}(\omega_1, \omega_2) \sqrt{s_H(\omega_1)} \sqrt{s_V(\omega_2)} e^{-i(\omega_1 - \omega_2)\tau} \\ &\quad - \mathcal{C}(\omega_2, \omega_1) \sqrt{s_H(\omega_2)} \sqrt{s_V(\omega_1)}|^2 \\ &\quad + \frac{1}{4} \iint d\omega_1 d\omega_2 |\mathcal{C}(\omega_1, \omega_2) \sqrt{1 - s_H(\omega_1)} \sqrt{1 - s_V(\omega_2)} e^{-i(\omega_1 - \omega_2)\tau} \\ &\quad - \mathcal{C}(\omega_2, \omega_1) \sqrt{1 - s_H(\omega_2)} \sqrt{1 - s_V(\omega_1)}|^2, \end{aligned} \quad (13)$$

$$\begin{aligned} P_{c,\text{bunch}} &= P_{VH} + P_{HV} \\ &= 2 \frac{1}{4} \iint d\omega_1 d\omega_2 |\mathcal{C}(\omega_1, \omega_2) \sqrt{s_H(\omega_1)} \sqrt{1 - s_V(\omega_2)} e^{-i(\omega_1 + \omega_2)\tau} \\ &\quad - \mathcal{C}(\omega_2, \omega_1) \sqrt{1 - s_H(\omega_2)} \sqrt{s_V(\omega_1)}|^2. \end{aligned} \quad (14)$$

The first term $P_{c,\text{sep}}$ defines the envelope of the HOM interferogram while the the second term $P_{c,\text{bunch}}$ is a rapidly oscillating term resulting from Franson-type interference between the two paths of the interferometer. In Fig. S3 (b-d), we display the simulated coincidence probability for different values of the TE and TM (H and V) splitting ratios. We observe that in all three cases the general shape of the interferogram follows a typical HOM dip with a background oscillating at a temporal period of 3 fs, which cannot be resolved by our free-space delay line. Hence when measuring the experimental HOM coincidence probability $P_{c,\text{exp}}$, these oscillations reduce to a constant background given by the average value of the oscillating term over a temporal window of 30 fs defined by the resolution of our free-space delay line : $P_{c,\text{exp}} = \bar{P}_{c,\text{bunch}} + P_{c,\text{sep}}$. The simulated value for $P_{c,\text{exp}}$ is shown in Fig. S3 (b-d)

as a solid red line. We note that, in agreement with experimental results, the visibility drops from $V = 89\%$ to $V = 80\%$ when going from $s_H = s_V = 1$ (Fig. S3 (d)) to the experimental values $s_H(\omega), s_V(\omega)$ of the splitting ratios (Fig. S3 (c)). As can be seen from our model this decrease can be attributed to the imperfect polarization splitting which gives a non-zero contribution to $P_{c,\text{bunch}}$ subsequently lowering the HOM visibility.

References

- (1) Autebert, C.; Bruno, N.; Martin, A.; Lemaitre, A.; Carbonell, C. G.; Favero, I.; Leo, G.; Zbinden, H.; Ducci, S. Integrated AlGaAs source of highly indistinguishable and energy-time entangled photons. *Optica* **2016**, *3*, 143.
- (2) Appas, F.; Baboux, F.; Amanti, M. I.; Lemaître, A.; Boitier, F.; Diamanti, E.; Ducci, S. Flexible entanglement-distribution network with an AlGaAs chip for secure communications. *npj Quantum Inf.* **2021**, *7*, 117.
- (3) Brańczyk, A. M. Hong-Ou-Mandel Interference. **2017-10-31**, arXiv:1711.00080v1.